Kinetics of breakaway oxidation of Fe–Cr and Fe–Cr–Ni alloys in dry and wet carbon dioxide

Thomas Gheno, Daniel Monceau, David J. Young

Kinetics of breakaway oxidation of Fe–Cr and Fe–Cr–Ni alloys in dry and wet carbon dioxide

Thomas Gheno[1,2], Daniel Monceau[1] and David J. Young[2*]

[1] *Institut Carnot CIRIMAT, ENSIACET, 31030 Toulouse Cedex 4, France*
[2] *School of Materials Science and Engineering, The University of New South Wales, Sydney, NSW 2052, Australia*

This is a post-peer-review, pre-copyedit version of an article published in Corrosion Science. The final version is available online at: https://doi.org/10.1016/j.corsci.2013.08.008

Abstract. Model Fe–Cr and Fe–Cr–Ni alloys were reacted in Ar–CO_2 and Ar–CO_2–H_2O gas mixtures at 650 °C. Initially protective oxidation, due to Cr_2O_3 formation, was usually followed by a transition to rapid oxidation, associated with Fe-rich oxide nodule development. Nodule surface coverage and overall weight gains are modelled on the basis of continued nucleation of nodules, and their diffusion-controlled growth. In general, water vapour accelerated nucleation. Alloying with nickel decreased average nucleation rates, but austenitic alloys showed large variations in nucleation susceptibility with grain orientation. Slower nodule growth induced by high chromium and nickel levels counteracted the effects of frequent nucleation.

Keywords: Steel; High temperature corrosion; Selective oxidation

1 Introduction

The current development of technologies aimed at reducing carbon dioxide emissions from coal combustion, such as oxyfuel firing, involves handling hot CO_2–H_2O gas mixtures, and raises concerns as to the oxidation resistance of steels employed as piping or heat exchanger materials in these environments. While the oxidation of steels in CO_2- or H_2O-rich gases has been extensively documented, reaction in gas mixtures containing large amounts of both species has not been well investigated.

Chromium-bearing steels used in these applications are subject to breakaway: the transition from protective oxidation, due to the exclusive formation of a Cr_2O_3 scale, to fast oxidation, characterised by the rapid growth of iron-rich oxides. The loss of protective properties is known to be accelerated in the presence of CO_2 [1–3], H_2O [4–9], and in CO_2–H_2O [2, 3] atmospheres, as compared to air or oxygen.

Breakaway is defined as a rapid increase in the oxidation rate. This can be manifested in a variety of reaction morphologies, depending on alloy composition. In the case of steels, and also of Ni-base alloys, the associated morphological evolution is non-uniform, as it involves nucleation, spreading and thickening of oxide nodules on the alloy surface. In some cases, nodule growth is rapid and starts after a well defined incubation time [4, 6, 10], which may be conveniently used to compare the performance of alloys oxidised in various conditions. However, as the transition in the oxidation kinetics is continuous, it can sometimes be more difficult to define

*Corresponding author. Tel.: +61 2 9385 4322; fax: +61 2 9385 5956.
E-mail address: d.young@unsw.edu.au (D.J. Young).

an incubation period. Furthermore, breakaway is very sensitive to the experimental conditions of the exposure, such as specimen geometry [10], and kinetics have been reported to vary between apparently equivalent specimens reacted in the same conditions [11].

Iron oxide nucleation and growth rates contribute to the loss of oxidation resistance in different manners. Both should be taken into account: it may be preferable for a material to be prone to scale failure but form relatively slow-growing nodules, than to undergo less frequent nucleation events each leading to catastrophic metal loss. However, the characterisation of reaction kinetics accompanying breakaway oxidation has received little attention.

This paper is focused on the kinetic aspects of breakaway oxidation of Fe–Cr and Fe–Cr–Ni alloys in dry and wet CO_2 atmospheres at 650 °C. The effects of gas and alloy composition on the reaction kinetics are investigated, and alloy oxidation resistance is analysed on the basis of nucleation and growth rates of Fe-rich oxide nodules. The work forms part of a larger investigation, aspects of which have already been reported. Carburisation of Fe–Cr alloys in dry and wet CO_2 was studied in Ref. [12], while the mechanism of breakaway oxidation, and the interactions between selective oxidation and carburisation were addressed in Ref. [13].

2 Materials and experiments

Alloys of compositions Fe–20Cr, Fe–20Cr–10Ni, Fe–20Cr–20Ni, Fe–25Cr, Fe–25Cr–10Ni and Fe–25Cr–20Ni were prepared according to the procedure detailed in Ref. [13] (all compositions given in weight % unless specified). The phase constitution of the annealed materials was determined by XRD: the binary alloys were ferritic, the ternary alloys containing 20Ni fully austenitic, while the 10Ni ternaries were dual-phase α–γ. Time-lapse isothermal oxidation experiments were carried out in flowing Ar–20CO_2, Ar–20CO_2–5H_2O and Ar–20CO_2–20H_2O gas mixtures at a total pressure of about 1 atm using a vertical tube furnace, according to the procedure described in Ref. [13]. Linear gas flow rates were set at about 2 cm s^{-1}. Specimens were weighed before and after exposure using a precision balance, with an error of 0.1 mg. Continuous thermogravimetric analysis (TGA) was performed using a Setsys Evolution microbalance equipped with a Wetsys humidifying system, both from Setaram. The drift was measured by running experiments with no specimen in gas flows corresponding to the experimental conditions, and values lower than 3 µg h^{-1} were obtained.

3 Experimental results

3.1 Overview

After exposure to Ar–CO_2 and Ar–CO_2–H_2O, large differences in oxide development were clearly evident among the alloys, regardless of gas composition. Ternary alloys containing 25Cr (all alloy compositions given in wt. %) formed a thin, protective oxide scale (Fig. 1a). In contrast, binary alloys were prone to breakaway oxidation, with nodules of thick oxide (Fig. 1b) interrupting the thin, passivating oxide. Ternary alloys containing 20Cr were intermediate in behaviour, passivating some grains, but showing breakaway on others (Fig. 1c).

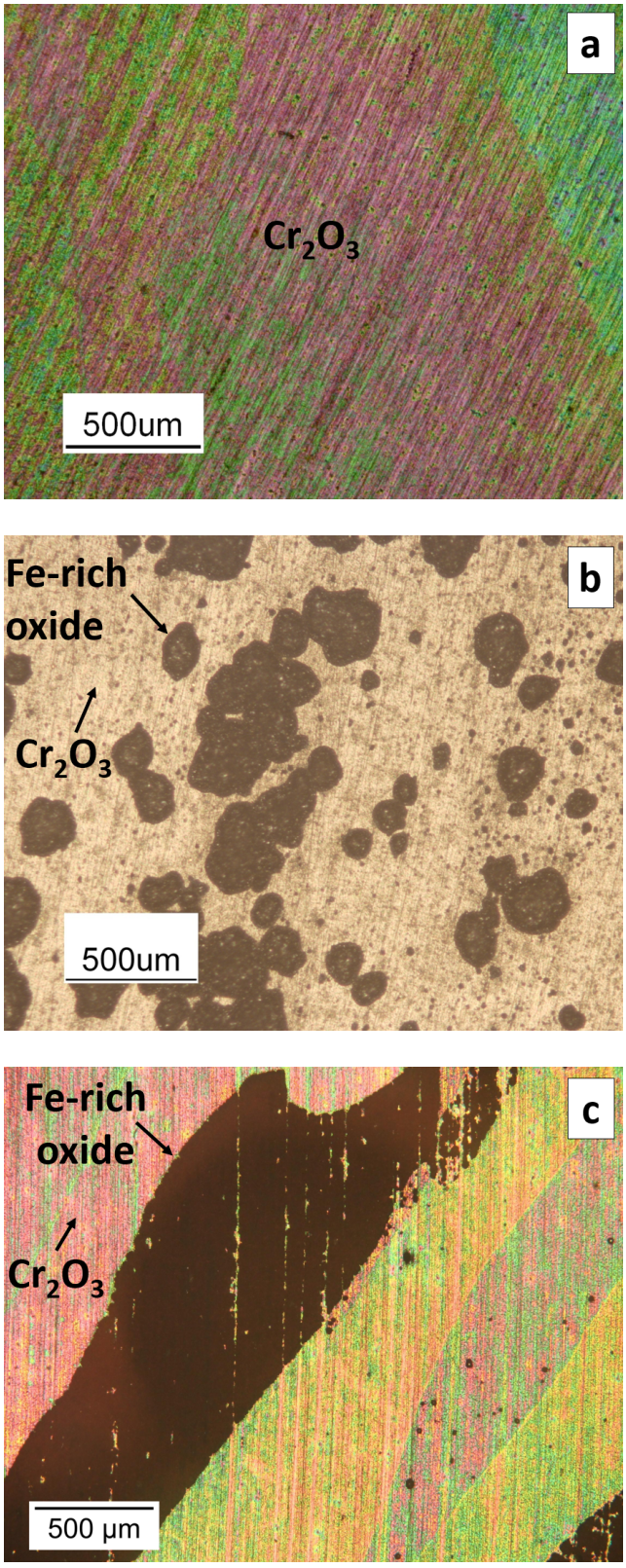

Figure 1: Surface view of samples after 120 h reaction. (a) Fe–25Cr–20Ni in Ar–20CO_2–20H_2O; (b) Fe–20Cr in Ar–20CO_2; (c) Fe–20Cr–20Ni in Ar–20CO_2–20H_2O.

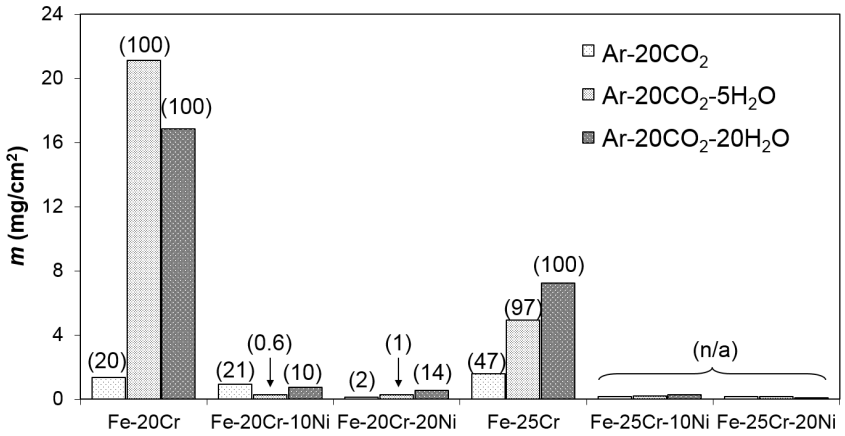

Figure 2: Weight gain per unit area and associated nodule surface area fraction (bracketed numbers, expressed in percent of the surface area) after 336 h reaction.

Surface area fractions of nodular oxide, θ, were measured by image analysis of reacted surfaces, using the ImageJ software [14]. Values of θ reflect the frequency of nodule formation and the rate at which they spread laterally, while weight gains also include the effects of nodule thickening, protective scaling, partial spallation, and any contribution of internal reaction. Spallation affected the protective scale and part of the thick nodules, both to variable extents. Net weight changes per unit area, m, and θ values measured after 336 h reaction are shown in Fig. 2. The binary alloys, Fe–20Cr and Fe–25Cr, underwent significant breakaway, accumulating relatively high weight gains. The extent of nodular growth on these alloys was larger in wet CO_2 than in dry CO_2, with nearly complete surface coverage by nodules in Ar–20CO_2–5H_2O and Ar–20CO_2–20H_2O. Ternary alloys with 20Cr and 10/20Ni showed limited breakaway, while those containing 25Cr evidenced no breakaway oxidation kinetics within the duration of these experiments.

3.2 Total weight gain and surface area fraction of Fe-rich oxide

Weight gain kinetics during exposure of Fe–20Cr to dry and wet CO_2 are shown in Fig. 3. Corresponding surface area fractions of nodular oxide, measured after each isothermal exposure, are presented in Fig. 4. The fact that m and θ values did not always increase monotonically with time indicates that the breakaway reaction was poorly reproducible from one specimen to another. This was particularly marked during exposure to the dry gas, where the extent of nodular growth was the lowest. In the gases containing 5 % and 20 % H_2O, all Fe–20Cr specimens reached high values of θ (> 80 %), even after short exposure times, resulting in higher weight gains than those measured in the dry gas. The extent of nodular growth did not differ significantly between the two wet gases.

In order to obtain self-consistent kinetic information during breakaway of the Fe–20Cr alloy, the time-lapse experiments were complemented by TGA experiments conducted in Ar–20CO_2 and Ar–20CO_2–5H_2O. Continuous weight gain curves are plotted together with the time-lapse results in Fig. 3, and θ values measured after these TGA experiments are included in Fig. 4. In the case of dry CO_2, the TGA

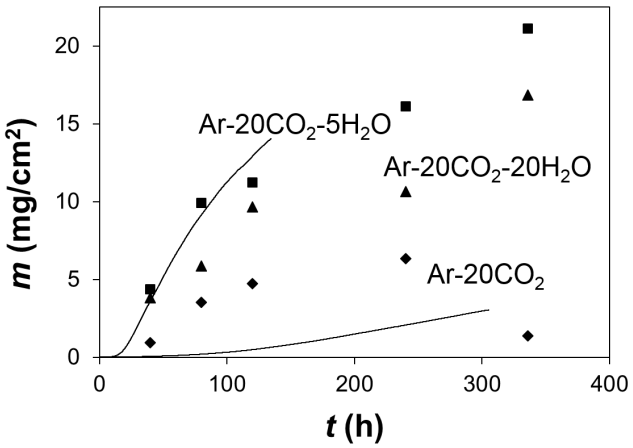

Figure 3: Weight change kinetics measured during reaction of Fe–20Cr. Markers: time-lapse experiments (each point represents a different specimen); solid lines: TGA experiments.

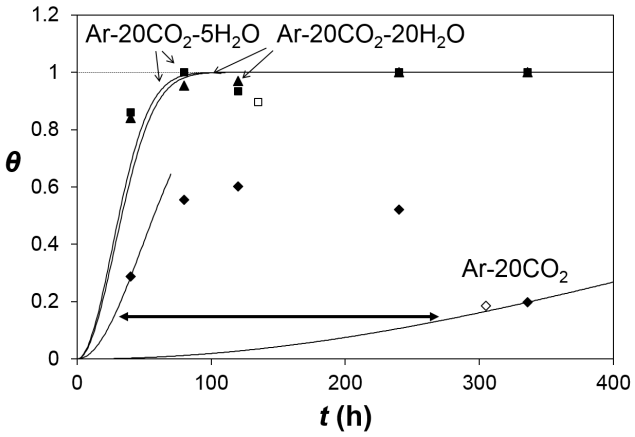

Figure 4: Surface area fractions of Fe-rich oxide for reaction of Fe–20Cr. Filled symbols: time-lapse experiments (each point represents a different specimen); open symbols: TGA experiments; solid lines: calculated from Eq. (7).

specimen yielded results which fell within the large range of variability defined by the time-lapse experiments. Reaction in Ar–20CO_2–5H_2O produced TGA results (m and θ) in agreement with the time-lapse measurements.

Early stage oxidation kinetics measured by TGA are shown in Fig. 5, together with those recorded during oxidation in dry air of an Fe–20Cr specimen taken from the same alloy batch. Short term reaction followed similar kinetics in all three gases. However, the rapid increase in weight gain after 2 h reaction in Ar–20CO_2–5H_2O indicates that the presence of H_2O in the reacting atmosphere accelerated the appearance of breakaway oxidation.

Time-lapse experiments on the Fe–25Cr alloy produced m and θ values qualitatively similar to those presented above for Fe–20Cr. The presence of H_2O(g) had the same effect, in that the extent of nodular growth was consistently high after reaction in Ar–20CO_2–5H_2O and Ar–20CO_2–20H_2O, but lower and more variable after

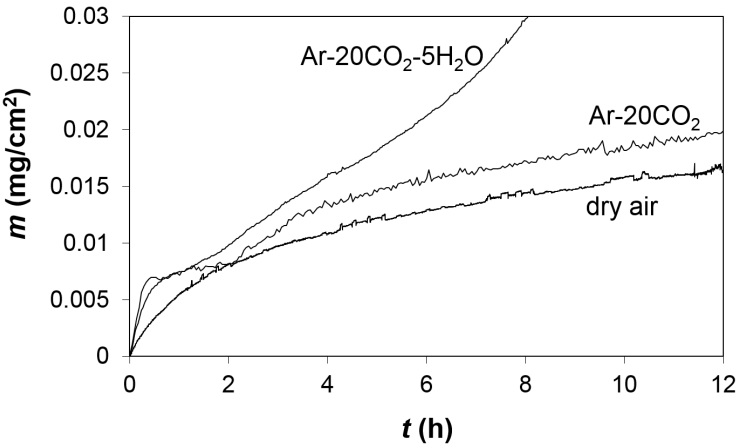

Figure 5: Early stage weight gain kinetics during oxidation of Fe–20Cr in dry and wet CO_2 and in dry air.

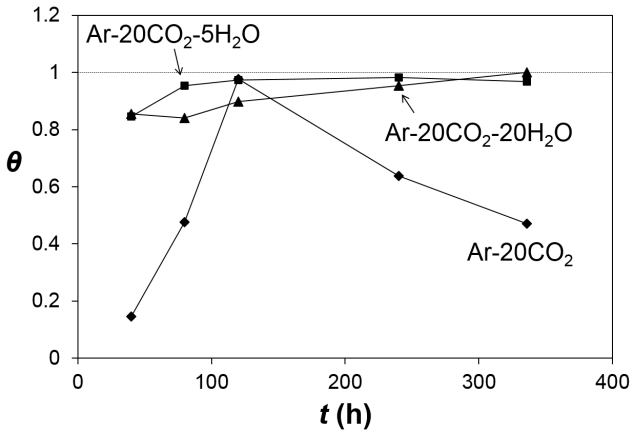

Figure 6: Surface area fraction of Fe-rich oxide measured for Fe–25Cr (time-lapse experiments; each point represents a different specimen).

exposure to Ar–20CO_2, as seen in Fig. 6, where each point represents a different specimen. The ternary alloys Fe–20Cr–10Ni and Fe–20Cr–20Ni also formed oxide nodules but m and θ values were lower than those measured on the binary alloys (Fig. 2). The data of Fig. 2 represent a single exposure time. Similar results obtained for a number of different reaction times of the 20Cr ternaries revealed considerable variability in m and θ values for all three gases. Surface area fractions measured on individual specimens after exposures of the Fe–20Cr–20Ni alloy are shown in Fig. 7. Correlations between m and θ values are obscured by the statistical spread of nodule nucleation rates; discussion returns to this point later. The 25Cr ternaries oxidised very slowly in dry and wet CO_2, at rates which could not be properly measured by the time-lapse technique. The weight uptakes recorded after each exposure did not exceed 0.4 mg cm^{-2}. These alloys formed some small isolated nodules (too small to be seen in Fig. 1a), covering a very small surface area fraction, which was not measured.

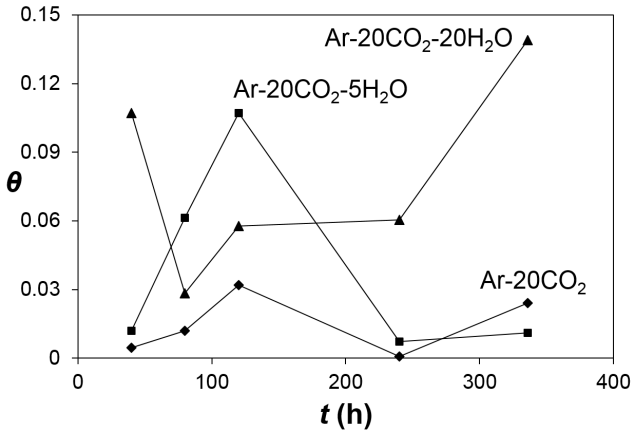

Figure 7: Surface area fraction of Fe-rich oxide measured for Fe–20Cr–10Ni (time-lapse experiments; each point represents a different specimen).

3.3 Iron-rich oxide growth rate

Nodule morphologies developed on the different alloys, described in detail in Ref. [13], are briefly recapitulated. The nodules formed on Fe–20Cr consisted of an outer part made up of iron oxide layers, and an inner part containing a mixture of Fe-rich and Cr-rich spinel oxide particles. In the nodules formed on Fe–20Cr–10Ni and Fe–20Cr–20Ni, the Fe-rich spinel was replaced by a Ni-containing spinel. The Fe–25Cr alloy produced two types of multilayer oxide: thick nodules like those formed on Fe–20Cr, and thinner, "healed" scales, which contained an inner Cr-rich layer. Intragranular carburisation of the binary alloys was extensive where Fe-rich nodules formed, and limited or absent beneath Cr_2O_3 and the healed scale. The Fe–20Cr–10Ni alloy formed only scattered intergranular carbides, and Fe–20Cr–20Ni and the 25Cr ternaries did not form any carbide. The gas composition had no significant influence on the carburisation rate measured for Fe–20Cr [12]. In the case of Fe–25Cr and Fe–20Cr–10Ni, however, the presence of H_2O(g) caused a decrease in the extent of carburisation.

Nodule thickening kinetics measured for Fe–20Cr were described in Ref. [13] using the parabolic law

$$X^2 = 2k_{p,\mathrm{Fe-ox}}t \tag{1}$$

where X is the maximum nodule thickness and $k_{p,\mathrm{Fe-ox}}$ the parabolic rate constant. The gas composition had no significant influence on the rate constant. Values of $k_{p,\mathrm{Fe-ox}}$ were estimated using a limited number of specimens of the three other alloys prone to breakaway oxidation. In the case of Fe–25Cr, the kinetics were measured for both types of iron-bearing scale. Values of $k_{p,\mathrm{Fe-ox}}$ obtained this way are listed in Table 1, reproduced from Ref. [13].

Since nodules grown on a given specimen have varying sizes (Fig. 1), measuring the maximum thickness observed on a cross-section would produce non-representative results. In the case of Fe–20Cr, these results were for this reason compared with rate constants obtained from weight gain measurements. Considering the fact that extensive carburisation did not occur below Cr_2O_3, the total weight gain per unit area m may be expressed so as to reflect the contribution of Fe-rich

Table 1: Fe-rich oxide thickening rate constant, $k_{p,\mathrm{Fe-ox}}$ (10^{-11} cm^2 s^{-1}) (reproduced from [13]).

	Ar–20CO_2	Ar–20CO_2–5H_2O	Ar–20CO_2–20H_2O
Fe–20Cr	12	12	8.5
Fe–20Cr–10Ni	3.1		
Fe–20Cr–20Ni			1.0
Fe–25Cr (thick nodules)	6.7		5.1
Fe–25Cr (healed scale)	0.069		0.069

oxide, carbides and Cr_2O_3:

$$m = \theta(m_{\mathrm{Fe-ox}} + m_{\mathrm{MC}_\nu}) + (1-\theta)m_{\mathrm{Cr_2O_3}} \tag{2}$$

where m_i is the average weight uptake per unit area of the indicated phase. In the present experiments, orders of magnitude of the weight uptakes are calculated to be 10, 1 and 0.1 mg cm^{-2} for Fe-rich oxide, carbides and Cr_2O_3, respectively. Consequently, the contribution of the carbides and Cr_2O_3 to the total weight gain may be neglected, and Eq. (2) approximated as

$$m_{\mathrm{Fe-ox}} = \frac{m}{\theta} \tag{3}$$

Assuming that nucleation of Fe-rich oxide occurs initially, at $t = 0$, and not subsequently, the values of m and θ measured after time-lapse exposures may be used to estimate nodule growth kinetics. The variety of nodule sizes found on a given specimen (Fig. 1) shows that the hypothesis of exclusive initial nucleation is not valid. However, it allows a very simple quantitative treatment of weight gain kinetics, justified in Section 4.2 using a model which takes into account continued nucleation throughout the exposure. The values of $m_{\mathrm{Fe-ox}}$ calculated from Eq. (3) are plotted in Fig. 8, and confirm that nodule growth on Fe–20Cr followed approximately parabolic kinetics. The variability associated with breakaway prevents the influence of gas H_2O content from being clearly identified. For uniformly thick and dense oxide, gravimetric (k_w) and thickening (k_p) rate constants are related through [15]

$$k_w = \left(\frac{16b}{V_{\mathrm{M_aO_b}}}\right)^2 k_p \tag{4}$$

where $V_{\mathrm{M_aO_b}}$ is the molar volume of oxide M_aO_b. Approximating the average oxide as dense Fe_3O_4, the average gravimetric rate constant obtained from Fig. 8, $k_{w,\mathrm{Fe-ox}} = 1.2\times10^{-4}$ mg^2 cm^{-4} s^{-1}, is converted to a thickening constant $k_{p,\mathrm{Fe-ox}} = 6.1\times10^{-11}$ cm^2 s^{-1}, in reasonable agreement with the values given in Table 1 for Fe–20Cr. A difference between these values must emerge from the fact that nodules are ellipsoid, and not flat-topped. The error is maximum for small individual nodules, and decreases as nodules coalesce and form uniformly thick scales. Offsetting this error is the systematic underestimation of nodule thickness resulting from the fact that random cross-sections do not on average pass through nodule centres.

Iron-rich oxide growth kinetics on Fe–20Cr were estimated in a third independent way. The local fitting procedure described in Ref. [16] was applied to the TGA

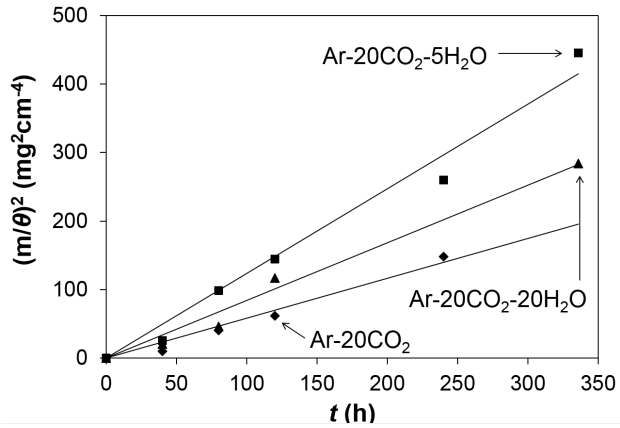

Figure 8: Iron-rich oxide growth kinetics for Fe–20Cr (time-lapse experiments; each point represents a different specimen), expressed in terms of corrected weight gains defined in Eq. (3).

data recorded during reaction in Ar–20CO_2–5H_2O, in order to determine the instantaneous gravimetric rate constant during the whole reaction. The rate constant is calculated according to

$$t = a + b\,m + c\,m^2 \tag{5}$$

where a and b are constants, and $c = \frac{1}{2k_w}$. This procedure allows a correct determination of k_w during a parabolic regime which follows a transient regime with different kinetics [16]. The resulting curve $k_w = f(t)$, shown in Fig. 9, is divided into three regions. Initially, as θ is low, the weight gain reflects Cr_2O_3 growth, and accordingly k_w is very small. After a first inflection in the weight gain curve (visible at $t \approx 2$ h in Fig. 5), and as θ and m rapidly increase, k_w is not defined (parabolic rate constants do not apply to convex weight gain functions). After a second inflection point, a second stage of parabolic kinetics is reached, and k_w attains a constant, high value. Using the molar volume of Fe_3O_4, the gravimetric constant obtained this way is converted to $k_p = 1.9 \times 10^{-10}$ cm^2 s^{-1}, a value consistent with that given in Table 1 for the directly measured rate constant of Fe-rich oxide grown on Fe–20Cr.

4 Kinetics modelling

The effects of alloy and gas compositions on breakaway oxidation are usefully considered within the framework of a reaction mechanism. As is clear from the present results and those already presented [13], the mechanism of breakaway is qualitatively similar for all alloys investigated: nucleation and growth of iron-rich oxide nodules, as a result of local failure of the initially formed Cr_2O_3 scale. As the nodule thickening and spreading rates are related [13], only one growth process needs to be considered.

Questions of importance in a kinetic description therefore concern the relative contributions of nucleation and growth, the uniformity or otherwise of these processes over a specimen surface, and their reproducibility from specimen to specimen. To be useful, any kinetic description needs to encompass the way in which each of

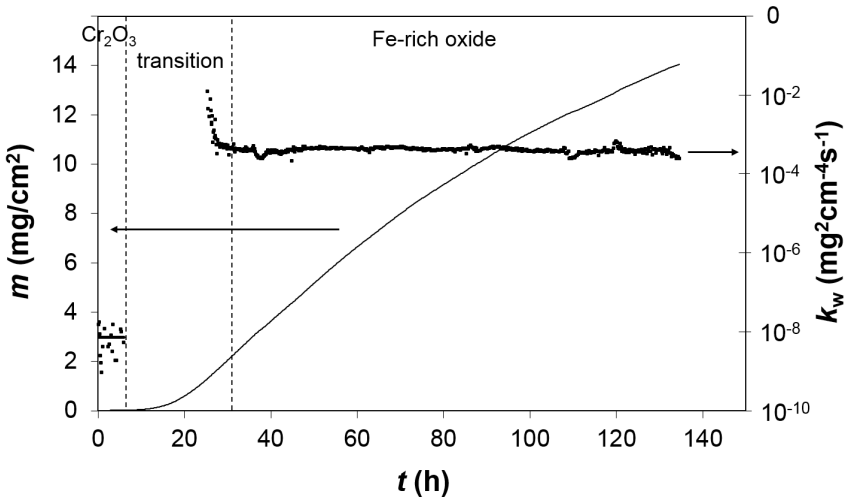

Figure 9: Weight gain measured by TGA during oxidation of Fe–20Cr in Ar–20CO_2–5H_2O and local gravimetric rate constant, determined after method in Ref. [16].

the nucleation and growth processes is affected by alloy chromium and nickel levels, and water vapor.

A starting point is provided by the assumption that nucleation is a random event, occurring with equal probability on any alloy surface where a chromia scale is still present. This simplifying assumption allows the application of classical phase transformation kinetic theory in developing an expression for surface coverage as a function of exposure time. A numerical model is then developed for the purpose of summing the weight uptake contributions of all nodules, and arriving at the overall kinetics of weight uptake.

4.1 Model for nucleation-spreading of Fe-rich nodules

The surface area fraction of Fe-rich oxide, θ, reflects both the frequency of nodule nucleation, and the rate at which they spread laterally. Evans [17] proposed a simple mathematical treatment of the problem of a surface covered by films spreading out as expanding circles. In the present case, individual nodules were approximately circular in plan (Fig. 1). As nodules observed on a given specimen surface had varying sizes, it is assumed that nucleation occurs continuously until complete surface coverage is reached. In the case of the 20Cr ternary alloys, surface coverage varied greatly according to grain orientation (Fig. 1c). However, since available experimental data reflect nodule development on entire specimens, nucleation-growth kinetics can only be described in an overall way, reflecting average behaviour. Similarly, the influence of specimen edges and suspension holes is disregarded. It is thus assumed that nucleation events, which occur on the still uncovered portion, are independent in time and position. In earlier work [13], nodule lateral growth kinetics were described as

$$r^2 = 2k_l\, t \tag{6}$$

where r is the nodule radius, k_l the lateral growth rate constant ($k_l = 0.73\, k_{p,\mathrm{Fe-ox}}$ for all alloys and gases), and t is the time elapsed since an individual nodule nucleated.

Taking this rate law into account, Evans' analysis [17] is adapted to yield

$$\theta = 1 - \exp\left(-\pi\Omega k_l t^2\right) \tag{7}$$

where Ω is the number of nuclei formed per unit of surface area and time, or nucleation rate. It is noted that Eq. (7) is a particular case of Avrami (or Kolmogorov-Johnson-Mehl-Avrami) kinetics [18]. In particular, the fact that expanding nodules eventually overlap is accounted for.

Applicability of the uniform nucleation hypothesis, where Ω is constant in time and space, to nodule development kinetics is first assessed by examining the evolution of θ with reaction time. As seen in Fig. 4, the evolution of θ values measured after reaction of Fe–20Cr in Ar–20CO_2 cannot be represented using a single monotonic function of time. This reflects of lack of reproducibility between different specimens of the same composition, a problem discussed in Section 5.1. Similarly, surface area fractions recorded after exposure of the Fe–25Cr alloy in Ar–20CO_2 (Fig. 6), and of the 20Cr ternary alloys in all gases (see Fig. 7 for Fe–20Cr–20Ni), cannot be described using a single nucleation rate.

Reaction of the binary alloys in wet CO_2, however, led to consistently high θ values (Figs. 4 and 6). The general form of Eq. (7) is then examined by representing $\ln 1 - \theta$ as a function of t^2, as shown in Fig. 10. Cases for which $\theta = 1$ cannot be taken into account, and are omitted. In this semi-log representation, Eq. (7) corresponds to a straight line passing through the origin of coordinates (0, 0), with a slope proportional to Ω. Although the small number of experimental data points limits the precision of this analysis, θ values measured after reaction of the binary alloys in wet CO_2 are seen in Fig. 10 to be compatible with Eq. (7) for short reaction times. However, data recorded after longer reaction times deviate from the trend seen in early reaction: long term θ values seem to correspond to lower nucleation rates than those typical of shorter-term data. This deviation might be rationalised by considering the possibility that after a stage of relatively rapid nodule development, complete surface coverage is not reached as fast as predicted in the situation of uniform nucleation depicted by Eq. (7). As seen in Figs. 4 and 6, the last 5 % or so of the specimen surfaces would thus appear to resist nodule coverage to an unexpected degree. However, whether any systematic delay in achieving complete surface coverage actually existed is obscured by the significant variability of the data. In order to circumvent the lack of reproducibility between different specimens, continuous weight gains measured by TGA during exposure of Fe–20Cr (Fig. 3) are now used to evaluate θ throughout the reaction of a single specimen.

4.2 Model for nucleation–spreading–thickening of nodules

Weight gain kinetics arising from nucleation and growth of oxide nodules during breakaway oxidation were analysed by Cox et al. [11] using a relation equivalent to Eq. (2). However, weight gain and nodule surface coverage kinetics can only be related through Eq. (2) if nucleation occurs initially, at $t = 0$, and not subsequently. In the present situation, the observation of nodules of significantly different sizes at a given time shows that nucleation continues throughout the reaction until surface coverage is complete. As represented schematically in Fig. 11, the total weight uptake at any given time then depends on the nodule "age" (or size) distribution, and not solely on the total surface area fraction θ. The Fe-rich oxide thickness at

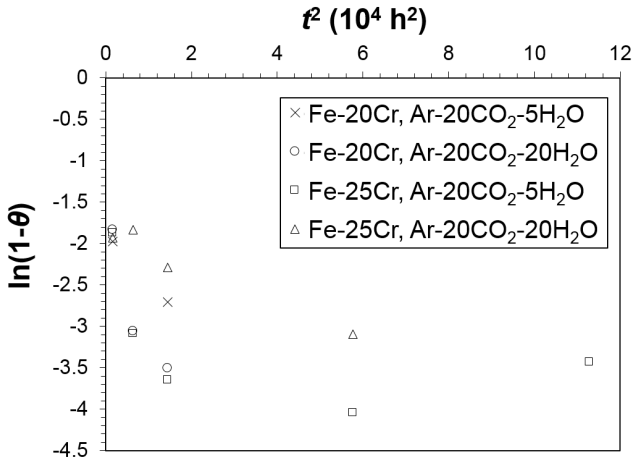

Figure 10: Semilog representation of the surface area fractions of Fe-rich oxide measured after reaction of the Fe–20Cr and Fe–25Cr alloys in wet CO_2 (time-lapse experiments; each point represents a different specimen).

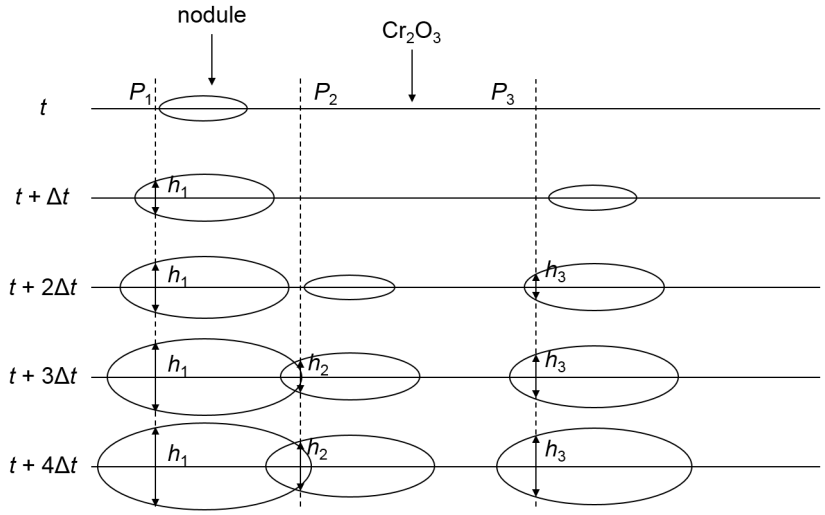

Figure 11: Scheme representing an alloy cross-section during a continuous nucleation–growth process. A nodule reached $P1$ between t and $t+\Delta t$, while $P3$ was covered between $t+\Delta t$ and $t+2\Delta t$, and $P2$ between $t+2\Delta t$ and $t+3\Delta t$. The relation $h_i^2 = 2k_{p,\mathrm{Fe-ox}}(t-t_i)$ applies to all three points, and at any given time $h_1 > h_3 > h_2$.

any given point on the surface is determined by the time elapsed since an expanding nodule reached this point. In order to model weight gain kinetics, a statistical approach is presented, based on the probability that any given point is covered by Fe-rich oxide in a given time interval. This analysis is constructed on the basis of the statistical model for oxide scale spallation during thermal cycling presented in Ref. [19].

Weight gain kinetics for uniform Fe-rich oxide growth are described using a simple parabolic law:

$$m_{\mathrm{Fe-ox}}^2 = 2k_{w,\mathrm{Fe-ox}}t \tag{8}$$

Time is then described as a discrete quantity: $t = n\Delta t$, where n is a positive integer and Δt a fixed time step. Thus the weight gain accumulated by a uniform scale from step 1 to step n, $M_n = m(t = n\Delta t)$, is written

$$M_n = M_1\sqrt{n} \tag{9}$$

with $M_1 = \sqrt{2k_{w,\mathrm{Fe-ox}}\Delta t}$. The weight gain due to carbides and Cr_2O_3 is neglected at this stage. If a point P on the surface is covered by a nodule at the beginning of the high temperature exposure, i.e. during the first time step, the "local" weight uptake at point P during the n^{th} time step is

$$\Delta M_{1n} = M_1\left(\sqrt{n} - \sqrt{n-1}\right) \qquad \text{for } n \geq 1 \tag{10}$$

The surface area fraction of Fe-rich oxide, $\theta(t)$, is the cumulative distribution function for surface coverage. Hence the probability that point P is reached by a nodule before time step i is $\theta(i\Delta t)$, denoted by θ_i. Therefore, the probability that point P is covered during time step i, that is between $t = (i-1)\Delta t$ and $t = i\Delta t$, is $\theta_i - \theta_{i-1}$, for $i \geq 1$. If a nodule reached P during time step i, the weight uptake at point P during the n^{th} time step is

$$\Delta M_{in} = M_1\left(\sqrt{n-i+1} - \sqrt{n-i}\right) \qquad \text{for } n \geq i \tag{11}$$

The total weight uptake during time step n, ΔM_n, is then calculated by adding, for every step i, the product of the probability that P was reached by a nodule during step i and the associated weight gain:

$$\begin{aligned}\Delta M_n = {} & \theta_1 M_1\left(\sqrt{n} - \sqrt{n-1}\right) + (\theta_2 - \theta_1)\, M_1\left(\sqrt{n-1} - \sqrt{n-2}\right) + \ldots \\ & + (\theta_i - \theta_{i-1})\, M_1\left(\sqrt{n-i+1} - \sqrt{n-i}\right) + \ldots \\ & + (\theta_n - \theta_{n-1})\, M_1 \qquad \text{for } n \geq 1\end{aligned} \tag{12}$$

The first term is related to areas covered by nodules during the first time step, leading to a minimum weight uptake during time step n; the last term represents areas covered by nodules during time step n. The probability that point P has not yet been covered by any nodule at time step n is $1 - \theta_n$. The corresponding weight gain is zero, as the contribution of Cr_2O_3 is neglected at this stage. Thus, provided that $\theta_0 = 0$, the fact that

$$\sum_{i=1}^{n}(\theta_i - \theta_{i-1}) + 1 - \theta_n = 1 \qquad \text{for } n \geq 1 \tag{13}$$

proves that all possible events have been taken into account in Eq. (12).

Chromia is assumed to grow according to parabolic kinetics:

$$m^2_{Cr_2O_3} = 2k_{w,Cr_2O_3}t \tag{14}$$

The hypothesis is reasonable in view of the early stage kinetics results presented in Fig. 5. The relative contribution of Cr_2O_3 to the total weight gain is significant in early reaction times, where the surface covered by nodules is relatively small. Since relevant $k_{w,\mathrm{Fe-ox}}$ values are four orders of magnitude larger than k_{w,Cr_2O_3}, this contribution becomes negligible quite rapidly after breakaway has started. Thus, the

accumulated weight gain at time step N, which is the quantity measured experimentally, may be approximated as

$$m_N = \sqrt{2k_{w,Cr_2O_3}N\Delta t} + \sum_{n=1}^{N} \Delta M_n \qquad \text{for } N \geq 1 \tag{15}$$

which in combination with Eq. (12) yields

$$m_N = \sqrt{2k_{w,Cr_2O_3}N\Delta t} + \sum_{n=1}^{N}\sum_{i=1}^{n} \left[\Delta\theta_i \sqrt{2k_{w,Fe-ox}\Delta t}\left(\sqrt{n-i+1} - \sqrt{n-i}\right)\right] \qquad \text{for } N \geq 1 \tag{16}$$

with $\Delta\theta_i = \theta_i - \theta_{i-1}$. Here the surface area fraction associated with chromia scale is omitted: the term is dominant when $\theta \approx 0$, but quickly becomes negligible as θ increases.

Although no assumption was made as to the distribution of nucleation events in time or space, that is, on the way in which θ evolves with time, the general form Eq. (16) relates total weight uptake to nodule coverage, provided only that k_{w,Cr_2O_3} and $k_{w,Fe-ox}$ are known. The equation is then used to determine θ from weight gains recorded by TGA during exposure of Fe–20Cr to Ar–20CO_2–5H_2O, according to the following procedure. Since the weight gain at any given time depends on the nodule size distribution, and consequently on all past θ values, Eq. (16) was solved for $\Delta\theta$ numerically: step by step, $\Delta\theta_i$ was evaluated so that the calculated weight gain matched the experimental weight gain, using all previously determined $\Delta\theta_i$ values. The computation was performed with Mathematica version 8.0 [20]. A time step $\Delta t = 1$ h was used; this value was verified to be sufficiently small to have no effect on the results. The rate constant for Cr_2O_3 growth was determined from the early stage reaction kinetics measured by TGA (Fig. 5), which yielded $k_{w,Cr_2O_3} = 5.4 \times 10^{-9}$ mg^2 cm^{-4} s^{-1}.

The procedure yielded a series of $\Delta\theta_i$ values, used to obtain θ_i values with the assumption that $\theta_0 = 0$. The rate constant $k_{w,Fe-ox}$ was adjusted so that the value of θ calculated for $t = 135$ h, the duration of the TGA experiment, matched the value measured experimentally at the end of the reaction. This yielded $k_{w,Fe-ox} = 3.4 \times 10^{-4}$ mg^2 cm^{-4} s^{-1} or, again using the molar volume of Fe_3O_4, $k_{p,Fe-ox} = 1.7 \times 10^{-10}$ cm^2 s^{-1}, in reasonable agreement with the value determined from thickness measurements (Table 1).

Values of θ resulting from the application of Eq. (16), plotted in Fig. 12, follow an S-shaped curve, as expected for a nucleation-growth phenomenon. It is desirable to compare this curve to that obtained within the uniform nucleation rate hypothesis, Eq. (7), using nucleation and growth rates corresponding to the measured weight gains. This is done by replacing θ_i in Eq. (16) by the expression

$$\theta_i = 1 - \exp\left(-0.73\pi\Omega k_{p,Fe-ox} i^2 \Delta t^2\right) \tag{17}$$

where the observed [13] relationship $k_l = 0.73k_{p,Fe-ox}$ has been used. With the general shape of θ now set by Eq. (17), Eq. (16) was fitted to the TGA data recorded during exposure of Fe–20Cr to Ar–20CO_2–5H_2O by adjusting the product $\Omega k_{p,Fe-ox}$ and $k_{w,Fe-ox}$. A wide range of adjustable parameter combinations

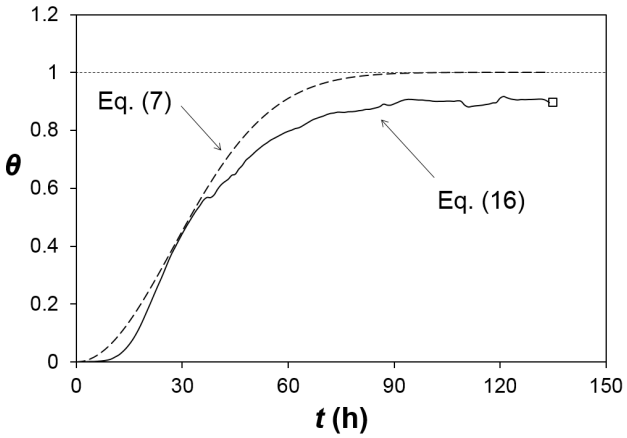

Figure 12: Surface are fraction of nodules during exposure of Fe–20Cr to Ar–20CO_2–5H_2O, obtained from TGA data and Eq. (16) (no hypothesis on the distribution of nucleation events), and from combined use of Eqs. (16) and (7) (uniform nucleation hypothesis). Details given in text.

Table 2: Nodule nucleation and growth rates from modelling TGA data for reaction of Fe–20Cr in Ar–20CO_2–5H_2O (k_p obtained from $k_{w,\mathrm{Fe-ox}}$ values via Eq. (4), using molar volume of Fe_3O_4).

	Numerical model Eqs. (16) and (17)	Approximate analytical model Eqs. (18) and (19)
$k_{w,\mathrm{Fe-ox}}$ (mg^2 cm^{-4} s^{-1})	2.7×10^{-4}	1.9×10^{-4}
$k_{p,\mathrm{Fe-ox}}$ (cm^2 s^{-1})	1.3×10^{-10}	9.4×10^{-11}
Ω (cm^{-2} s^{-1})	1.7×10^{-1}	1.3×10^{-1}

was explored in order to ensure that a global optimum in the fit was arrived at. The nucleation rate Ω was then obtained using the adjusted $k_{w,\mathrm{Fe-ox}}$ value, converted to a $k_{p,\mathrm{Fe-ox}}$ value via Eq. (4). Again, a time step $\Delta t = 1$ h and the value $k_{w,Cr_2O_3} = 5.4\times10^{-9}$ mg^2 cm^{-4} s^{-1} were used. The value of $k_{p,\mathrm{Fe-ox}}$ obtained from this optimisation procedure is seen in Table 2 to be in reasonable agreement with that determined from time-lapse experiments for Fe–20Cr in Ar–20CO_2–5H_2O (Table 1). Furthermore, the agreement between the optimised and experimental weight gains is excellent (Fig. 13).

Substitution of the adjusted values of Ω and $k_{w,\mathrm{Fe-ox}}$ in Eq. (7) yields the curve plotted in Fig. 12, where it is compared with that obtained from Eq. (16) alone. It is seen that θ values derived from TGA data via Eq. (16), where no constraint was placed on the distribution of nucleation events, deviate from uniform nucleation-spreading kinetics (Eq. (7)). Toward the end of the experiment, θ reaches a nearly constant level, despite the fact that coverage is not complete. However, the general shape of this θ curve is quite similar to that expected from the uniform nucleation hypothesis. This is an important observation, the consequences of which are discussed in Section 5.1.

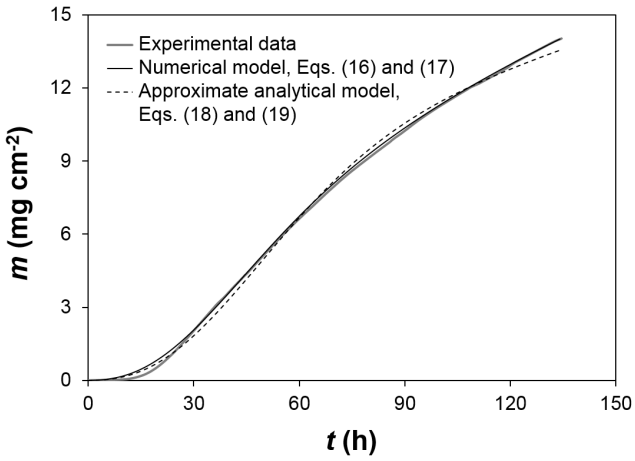

Figure 13: Experimental (TGA) and fitted weight gains for oxidation of Fe–20Cr in Ar–$20CO_2$–$5H_2O$. Fitted values obtained from optimisation of numerical model (Eqs. (16) and (17)) and approximate analytical model (Eqs. (18) and (19)).

4.3 Simplified modelling

Although the two numerical optimisation procedures presented above proved successful in simulating weight gain kinetics arising from continuous nucleation and growth of Fe-rich oxide, their scope of application is restricted by the non-algebraic form of Eq. (16). A simpler model is readily obtained by estimating weight uptake with the approximation that nodules nucleate at time zero and spread as flat-topped islands:

$$m(t) = (1 - \theta(t))\sqrt{2k_{w,\mathrm{Cr_2O_3}}t} + \theta(t)\sqrt{2k_{w,\mathrm{Fe-ox}}t} \tag{18}$$

However, the form of $\theta(t)$ is found by retaining the hypothesis of continuous nucleation, and rephrasing Eq. (17) as a continuous function:

$$\theta(t) = 1 - \exp\left(-0.73\pi\Omega k_{p,\mathrm{Fe-ox}}t^2\right) \tag{19}$$

Again the growth of both Cr_2O_3 and Fe-rich oxide is described with a simple parabolic law, and the contribution of carburisation to weight change is neglected.

The approximate analytical expressions, Eqs. (18) and (19), were fitted to the TGA data recorded during oxidation of Fe–20Cr in Ar–$20CO_2$–$5H_2O$ according to the procedure described above for the numerical model of Eqs. (16) and (17). The corresponding weight gains are plotted as a dashed line in Fig. 13. Values of the optimised parameters Ω and $k_{w,\mathrm{Fe-ox}}$ are seen in Table 2 to be in reasonable agreement with those obtained from the numerical model.

It is recognised that the hypotheses underlying Eqs. (18) and (19), initial and continuous nucleation, respectively, are mutually exclusive. The relative success of the approximate analytical model, which combines Eqs. (18) and (19), in simulating weight gain kinetics in a situation of continuous nucleation (Fig. 13 and Table 2), is related to the parabolic nature of nodule growth kinetics. As growth rates continually decrease, the contribution of smaller, newer nodules to the total weight uptake tends to catch up with that of larger, older nodules. Furthermore, as the reaction proceeds and θ increases, less surface is available for new nucleation events. It is

also acknowledged that simultaneous lateral growth and thickening of flat topped nodules is not realistic. Again, this contradiction is rationalised by considering the fact that nodules which grow according to parabolic kinetics and coalesce tend to form uniformly thick scales.

Comparison of the simulated weight gains in Fig. 13 indicates that the numerical model is better adapted than the approximate analytical model. It allows a more accurate fitting of the experimental data, while using the same number of adjustable parameters. The error made when applying the approximate model is now evaluated. Both models use the same expression to define the evolution of θ with time (Eq. (17) or the equivalent Eq. (19)), but they inevitably yield different values of the nucleation and growth parameters. Thus, the relative difference in the time needed to reach any given θ value is found from Eq. (19) to be

$$\frac{\Delta t}{t} = \frac{t_{\text{approx}} - t_{\text{num}}}{t_{\text{num}}} = \sqrt{\frac{(k_{w,\text{Fe-ox}}\Omega)_{\text{num}}}{(k_{w,\text{Fe-ox}}\Omega)_{\text{approx}}}} - 1 \tag{20}$$

where the subscripts num and approx refer to the numerical and approximate model, respectively. The optimised values of Ω and $k_{w,\text{Fe-ox}}$ (Table 2) yield $\Delta t/t$ =35 %. Although it is not, strictly speaking, applicable to a situation of continuous nucleation, the analytical expression Eq. (18) provides a reasonable approximation to the experimental data. This provides an empirical basis for the use of the simple Eq. (3) for evaluating Fe-rich oxide growth kinetics from total weight gains.

5 Discussion

Nodule development on specimens of the same composition reacted in a given gas was seen in Section 3.2 to be subject to considerable variability, in agreement with previous investigators [10,11]. The use of models to describe θ and m kinetics allows the variability associated with breakaway oxidation to be analysed, and the effect of gas and alloy composition on nodule nucleation to be evaluated. The applicability of ideal nucleation-growth kinetics to TGA data, for which weight uptake information is available throughout the exposure, is discussed first.

5.1 Variability of nucleation

The constant nucleation rate numerical model used for optimisation of weight gain kinetics in Section 4.2 is based on two equations: Eq. (16) to relate weight gains to surface area fractions, with no constraint on the distribution of nucleation events, and Eq. (17) or its equivalent Eq. (7), which specifies the form of $\theta(t)$ resulting from the uniform nucleation hypothesis. When fitted to the weight gains recorded during exposure of Fe–20Cr to Ar–20CO_2–5H_2O, this model is in error in that it predicts a θ value approaching 1 at the end of the TGA experiment, whereas $\theta(t = 135\text{h})$ was measured to be 0.9 (Fig. 12). Nevertheless, application of Eq. (16) alone to the TGA data yields a surface coverage evolution that conforms rather well to the general form of Eq. (7), that is, to uniform nucleation-growth kinetics. Examination of the data presented in Fig. 12 reveals that the θ curve obtained from Eq. (7) can be scaled down to match that corresponding to Eq. (16). From the point of view of kinetic modelling, this explains why weight gains optimised on the basis of a

constant nucleation rate fit experimental data very well (Fig. 13). An explanation for this observation could be that nucleation was indeed uniform, but on only 90 % of the specimen surface. The implied ability of the remaining 10 % to resist nodule formation requires explanation. The alternative possibility of a lower nucleation rate can be rejected, because it would fail to match the form of the θ(t) curve.

Differences in nodule nucleation behaviour on a specimen surface must reflect inhomogeneities, such as the presence of grain boundaries or other defects, or of grains with particular crystallographic orientations. Accelerated chromium supply at the alloy grain boundaries is to be expected for austenitic materials at low temperatures, and has been observed to prevent (or at least delay) breakaway in the case of a 304 steel reacted at 600 °C [21]. It is questionable whether such an effect would be important for higher diffusivity ferritic alloys reacted at 650 °C, and it was not observed in the present study.

Grain orientation has been shown to affect the nature of the oxide formed on Fe–Cr alloys reacted in CO_2–1%CO at 600 °C [22]. During reaction of Fe–10Cr and Fe–20Cr single crystals in low pressure O_2 at 627 °C [23], (110) surfaces formed Cr-rich α–$Fe_xCr_{2-x}O_3$, whereas (100) surfaces formed spinel oxides, for both alloy compositions. In both Refs. [22,23], epitaxial relationships were invoked by the authors to explain the stabilisation of either rhombohedral or cubic oxide during the initial stage of oxidation. If substrate-oxide orientation relationships can determine the nature of the oxide initially formed, they might also affect the growth rate of the protective scale, or its propensity to suffer mechanical failure. However, nodule-free areas on the surface of the Fe–20Cr specimen used for the TGA experiment in Ar–$20CO_2$–$5H_2O$ did not seem, by visual inspection, to coincide with individual grains. Other sources of inhomogeneity, such as impurities or inclusions non-uniformly distributed on the metal surface, might have affected nodule nucleation.

Likewise, θ and m values measured after time-lapse experiments (Section 3.2) reflect differences in the surfaces of several specimens of the same composition, exposed to a given gas. In the case of the ternary austenitic alloys, the prevalence of a correlation between grain orientation and nodule density is clear, as seen in Fig. 1c. Grains still covered by Cr_2O_3 exhibit varying interference colours, which reflect differences in oxide thickness. While the reasons for varying oxide growth rate with grain orientation cannot be identified from the present work, the consequences in terms of protective oxide failure, and consequently nodule nucleation, are readily anticipated: growth rates affect the strain energy, which affects the propensity for mechanical failure, and the amplitude of chromium depletion, which controls the alloy ability to maintain and reform a protective scale.

It must be noted that the alloys used in the present work had large grains ($\sim$ 500 µm), and thus a small number of grains per specimen. In the case of the 20Cr ternary alloys, the strong correlation between grain orientation and nodule nucleation therefore resulted in a lack of statistical weight for θ and m measurements, and accounts for the large scatter in these variables after time-lapse experiments (see for example Fig. 7).

In the case of the binary alloys, the nodule distribution was more or less uniform. Variations of the nodule density according to grain orientation were sometimes observed to a small extent, but the large variability in θ and m recorded after reaction in dry CO_2 (Figs. 4 and 6) must have had some other source. Reaction of Fe–20Cr and Fe–25Cr in wet CO_2, however, yielded θ values which consistently approached

1 (Figs. 4 and 6). Variability in nodule development might have been obscured by the rather high propensity for nucleation due to the combined presence of CO_2 and H_2O in the gas. Alternatively, the deviation from uniform nucleation-growth kinetics identified for the TGA experiment may also have applied, to some extent, to the time-lapse exposures. The fact that θ values recorded after reaction of Fe–20Cr and Fe–25Cr in wet CO_2 are not perfectly represented by Eq. (7) (Fig. 10) could thus be related to the existence of areas exhibiting enhanced resistance to nodule development, in addition to variations in the nucleation rate.

5.2 Influence of alloy and gas composition on nucleation rate

The analysis of nodule surface coverage from continuous weight gain measurements was carried out using one set of TGA data (Fe–20Cr in Ar–20CO_2–5H_2O), that is, one single specimen. Values of θ and m measured after reaction of several specimens of the same composition in a given gas indicated that nodule development was subject to considerable variability (Section 3.2). It is recognised that this variability must emerge from differences in specimen surfaces, in turn causing heterogeneities in nucleation rate. However, on the basis of the analysis of TGA data, nucleation-growth kinetics may, for comparison purposes, be approximated as uniform for each specimen. Application of Eq. (7) to θ values measured after time-lapse exposures thus allow, for a given alloy-gas combination, an average nucleation rate to be calculated, and the variability of breakaway to be evaluated in terms of varying nucleation rate, that is, in terms of the rate at which the overall reaction accelerates.

Nucleation rates Ω are calculated in the following manner. For the binary alloy reactions in wet CO_2, the product $k_l\Omega$ is obtained from the slope of the line of best fit in Fig. 10. Data points corresponding to long term (240 and 336 h) exposure of Fe–25Cr, likely representative of locally enhanced resistance to nucleation rather than globally low nucleation rates, are omitted. In the case of the binary alloy reactions in dry CO_2 and of the ternary alloy reactions in all gases (omitted from Fig. 10), it is recognised that the nucleation rate varied considerably from one specimen to another. The product $k_l\Omega$ is then determined as the arithmetic average of values obtained from Eq. (7), using θ measured after the different reaction times. For each alloy, k_l is derived from the relationship [13] $k_l = 0.73k_{p,\mathrm{Fe-ox}}$, using $k_{p,\mathrm{Fe-ox}}$ values obtained from thickness measurements (Table 1). In the case of the Fe–25Cr alloy, θ values reflect the sum of two sorts of nucleation events, corresponding to the two types of scale formed after Cr_2O_3 failure. These components cannot be distinguished when measuring θ on the specimen surfaces. However, metallographic observations on cross-sections showed that the thinner type of scale (healed scale) represented a major proportion of the post-failure oxide products. The contribution of the thick nodules was neglected, and healed scale growth rates were used to determine nucleation rates.

Average nucleation rates for all alloys and gases are shown in Fig. 14, where the error bars indicate minimum and maximum values, and the poor reproducibility of breakaway oxidation is clear. For all alloys except Fe–20Cr–20Ni, water vapour is seen to increase average nucleation rates. Thus, while no significant effect was seen in terms of nodule growth rate (Table 1), the fact that H_2O(g) accelerates breakaway oxidation is related to the more frequent nucleation of Fe-rich oxide nodules. Chromia scales are known to grow faster in the presence of H_2O [24–26]. A higher

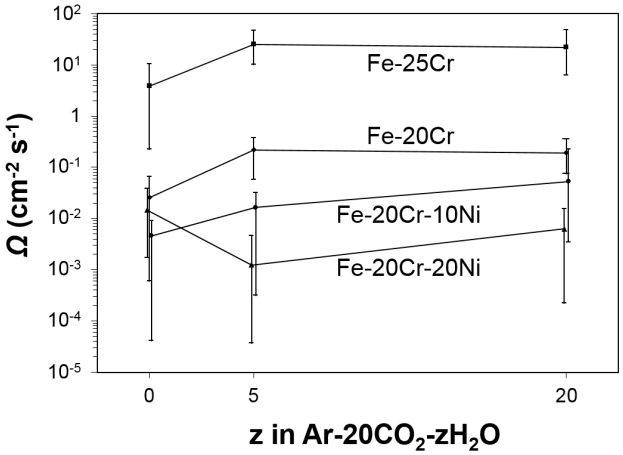

Figure 14: Nucleation rates resulting from the nucleation–spreading analysis (Eq. (7) applied to θ values measured after time-lapse experiments).

growth rate would indeed enhance chromium depletion, and favour non-selective oxidation after failure of the initial Cr_2O_3 scale. This could not be verified in the present work, as differences in Cr_2O_3 scale thickness between dry and wet CO_2 were no greater than local variations on a given specimen. The early stage oxidation kinetics measured by TGA in the case of Fe–20Cr (Fig. 5) did not indicate any difference in Cr_2O_3 growth rate between dry and wet CO_2. The presence of H_2O(g) must then have affected Cr_2O_3 growth without significantly altering the early stage kinetics.

The Fe–25Cr alloy is seen in Fig. 14 to evidence higher nucleation rates than the 20Cr alloys. Thus, while the higher chromium content allowed a temporary stage of relative protection to be reached after Cr_2O_3 failure, through the formation of a slow-growing, healed scale [13], it also led to more frequent Cr_2O_3 failure. No effect of alloy composition on Cr_2O_3 growth kinetics could be identified in the present study, because Cr_2O_3 thicknesses varied on a given specimen as much as they did among specimens of different compositions. However, studies conducted by previous investigators [27–29] on series of Fe–Cr alloys in dry or wet O_2 indicated that a minimum in Cr_2O_3 growth rate occurred for alloys containing about 15–20 wt. % Cr. This composition range was apparently valid for all temperatures tested, between 650 and 1000 °C. According to these data, Cr_2O_3 growth would thus be faster on Fe–25Cr than on Fe–20Cr. This is expected to result in higher scale failure frequency, and would account for the higher nucleation rates obtained for Fe–25Cr.

Nucleation rates calculated for the 20Cr ternary alloys were lower than those obtained for Fe–20Cr. However, this average result encompasses values which varied greatly with grain orientation. A complete range of oxidation behaviour was observed depending on grain orientation (Fig. 1c), from seemingly exclusive Cr_2O_3 formation to complete coverage by Fe-rich oxide. The fact that the influence of grain orientation was drastically enhanced for the Ni-bearing austenitic alloys is of interest, but could not be investigated from the present experimental results. In a situation where grain orientation is critical to nodule nucleation, analysing reaction

kinetics in terms of an average nucleation rate provides no insight into the reaction mechanism. From a practical standpoint, nickel additions slowed both average nucleation rates and nodule growth rates (Table 1), and thereby proved beneficial, as is evident from the lower weight gains (Fig. 2).

Nucleation rates determined for Fe–25Cr reaction in dry and wet CO_2 were significantly higher than those measured for Fe–20Cr (Fig. 14), but the higher chromium content allowed a relatively protective, "healed" type of scale to be formed after Cr_2O_3 failure on most of the surface. Local formation of thick Fe-rich oxide nodules was not avoided. However, as complete surface coverage by thick Fe-rich oxide was delayed by the availability of additional chromium, and its growth rate was lower for Fe–25Cr than for Fe–20Cr (Table 1), the overall effect of the higher chromium content was beneficial. This is also reflected in the total weight gains (Fig. 2).

Exclusive Cr_2O_3 growth was largely, but not fully, maintained in the case of the 25Cr ternaries, and small, scattered nodules did form. No measurements of nodule development were carried out. However, as discussed in Ref. [13], the nodule growth rate was certainly lower than those measured for the other alloys, as a result of combined chromium and nickel additions. Whatever the nucleation rate might have been, limited nodule growth allowed the total weight gains to remain typical of exclusive Cr_2O_3 formation (Fig. 2).

Chromia resistance to failure thus appears to be less critical than nodule growth rate in maintaining protective oxidation of the 25Cr ternary alloys at this relatively low temperature, 650 °C. As discussed in Ref. [13], the kinetic stability of Cr_2O_3 scales is intimately related to the outward flux of chromium to the metal/oxide interface. Although chromium lattice diffusion is faster in ferritic alloys than in austenitic alloys, short-circuit (grain boundary and dislocation) diffusion is likely to prevail in the slow diffusing γ phase at the low temperature of 650 °C [30]. The 10Ni alloys employed in the present study possess a fine $\alpha + \gamma$ structure, and in the fully austenitic 20Ni alloys, the effects of cold working in the subscale region are likely to be still present at 650 °C [31]. Short-circuit diffusion would then allow the chromium flux in the ternary alloys to approach that achieved in the binary alloys. This possibly explains why no great advantage was gained by the ferritic alloys in terms of nodule nucleation. However, the relative importance of the differing iron activies in the ferritic and austenitic alloys has not been established, and the question remains open.

6 Conclusions

While Cr_2O_3 scales formed on Fe–Cr and Fe–Cr–Ni alloys provide oxidation resistance, this protective behaviour can be disrupted by the development of Fe-rich oxide, which leads to rapid oxidation rates. During reaction in Ar–CO_2 and Ar–CO_2–H_2O at 650 °C, breakaway was observed to occur via nucleation and growth of Fe-rich oxide nodules.

The hypothesis of uniform nucleation was found to conform to measured nodule surface coverage kinetics only for short exposures of Fe–20Cr and Fe–25Cr in wet CO_2. Nodule development on Fe–20Cr–10Ni and Fe–20Cr–20Ni in all gases, and on the binary alloys in dry CO_2, was highly non-reproducible, to the extent that kinetics obtained from several specimens of a given composition could not be described using

a single nucleation rate.

A numerical procedure was developed to relate weight gains to surface area fractions of nodules. Application of this procedure to TGA data recorded during the exposure of Fe–20Cr to Ar–20CO_2–5H_2O allowed the evolution of θ during reaction to be determined. A deviation from uniform nucleation-growth kinetics was thus identified, and attributed to enhanced resistance to nucleation of part of the specimen surface.

Approximating nucleation as uniform, θ values recorded after time-lapse experiments were used to determine nucleation rates, allowing the extent and variability of breakaway to be evaluated.

Accelerated breakaway oxidation of binary alloys in wet CO_2 was shown to be due to more frequent nucleation of Fe-rich oxide, i.e. reduced resistance of Cr_2O_3 to failure, in the presence of H_2O(g), while nodule growth rates were insensitive to gas composition. Nucleation rates determined for Fe–25Cr were higher than those arrived at for Fe–20Cr, which was related to faster Cr_2O_3 growth on the Fe–25Cr alloy. However, increasing the chromium content also promoted the formation of low-diffusivity spinel oxides after Cr_2O_3 failure, which reduced nodule growth rates, and overall oxidation rates.

Nickel additions to Fe–20Cr had a complex effect, as they drastically enhanced the effect of grain orientation on nodule nucleation. This strong orientation effect, together with the large grain size of the alloys used, led to inadequate statistical sampling, preventing identification of gas composition and nickel concentration effects. However, reductions in both average nucleation rates and nodule growth rates provide a phenomenological explanation for the enhanced oxidation resistance of the Ni-bearing alloys.

Although nodules were formed on the 25Cr ternaries, their slow development yielded no marked acceleration in the reaction kinetics. The ability to sustain Cr_2O_3 formation was therefore less decisive than nodule growth rate in maintaining protective oxidation of these alloys. Oxidation resistance thus benefited from both chromium and nickel additions, which slowed nodule growth.

Acknowledgements

Financial support from the Australian Research Council Discovery program is gratefully acknowledged. The authors would like to thank Dominique Poquillon (CIRIMAT) for helpful discussions regarding numerical simulation of kinetics.

References

[1] C. S. Giggins and F. S. Pettit, Corrosion of metals and alloys in mixed gas environments at elevated temperatures, Oxidation of Metals 14 (1980) pp. 363–413. doi: 10.1007/BF00603609.

[2] J. Pirón Abellán, T. Olszewski, H. Penkalla, G. Meier, L. Singheiser and W. Quadakkers, Scale formation mechanisms of martensitic steels in high CO_2/H_2O-containing gases simulating oxyfuel environments, Materials at High Temperatures 26 (2009) pp. 63–72. doi: 10.3184/096034009X438185.

[3] G. H. Meier, K. Jung, N. Mu, N. M. Yanar, F. S. Pettit, J. Pirón Abellán, T. Olszewski, L. Nieto Hierro, W. J. Quadakkers and G. R. Holcomb, Effect of alloy composition and exposure conditions on the selective oxidation behavior of ferritic Fe–Cr and Fe–Cr–X alloys, Oxidation of Metals 74 (2010) pp. 319–340. doi: 10.1007/s11085-010-9215-5.

[4] I. Kvernes, M. Oliveira and P. Kofstad, High temperature oxidation of Fe–13Cr–xAl alloys in air–H_2O vapour mixtures, Corrosion Science 17 (1977) pp. 237–252. doi: 10.1016/0010-938X(77)90049-X.

[5] Y. Ikeda and K. Nii, Mechanism of accelerated oxidation of Fe–Cr alloys in water vapor containing atmosphere, Transactions of National Research Institute for Metals 26 (1984) pp. 52–62.

[6] S. Henry, A. Galerie and L. Antoni, Abnormal oxidation of stabilized ferritic stainless steels in water vapor, Materials Science Forum 369–372 (2001) pp. 353–360. doi: 10.4028/www.scientific.net/MSF.369-372.353.

[7] J. Ehlers, D. Young, E. Smaardijk, A. Tyagi, H. Penkalla, L. Singheiser and W. Quadakkers, Enhanced oxidation of the 9%Cr steel P91 in water vapour containing environments, Corrosion Science 48 (2006) pp. 3428–3454. doi: 10.1016/j.corsci.2006.02.002.

[8] E. Essuman, G. H. Meier, J. Żurek, M. Hänsel and W. J. Quadakkers, The effect of water vapor on selective oxidation of Fe–Cr alloys, Oxidation of Metals 69 (2008) pp. 143–162. doi: 10.1007/s11085-007-9090-x.

[9] N. K. Othman, J. Zhang and D. J. Young, Water vapour effects on Fe–Cr alloy oxidation, Oxidation of Metals 73 (2010) pp. 337–352. doi: 10.1007/s11085-009-9183-9.

[10] G. Wood and D. Whittle, The mechanism of breakthrough of protective chromium oxide scales on Fe–Cr alloys, Corrosion Science 7 (1967) pp. 763–782. doi: 10.1016/S0010-938X(67)80003-9.

[11] M. G. C. Cox, B. McEnaney and V. D. Scott, Kinetics of initial oxide growth on Fe–Cr alloys and the role of vacancies in film breakdown, Philosophical Magazine 31 (1975) pp. 331–338. doi: 10.1080/14786437508228936.

[12] T. Gheno, D. Monceau, J. Zhang and D. J. Young, Carburisation of ferritic Fe–Cr alloys by low carbon activity gases, Corrosion Science 53 (2011) pp. 2767–2777. doi: 10.1016/j.corsci.2011.05.013.

[13] T. Gheno, D. Monceau and D. J. Young, Mechanism of breakaway oxidation of Fe–Cr and Fe–Cr–Ni alloys in dry and wet carbon dioxide, Corrosion Science 64 (2012) pp. 222–233. doi: 10.1016/j.corsci.2012.07.024.

[14] T. J. Collins, ImageJ for microscopy, Biotechniques 43 (2007) pp. S25–S30. doi: 10.2144/000112517.

[15] N. Birks, G. H. Meier and F. S. Pettit, *Introduction to the High Temperature Oxidation of Metals*. Cambridge University Press 2nd ed. (2006).

[16] D. Monceau and B. Pieraggi, Determination of parabolic rate constants from a local analysis of mass-gain curves, Oxidation of Metals 50 (1998) pp. 477–493. doi: 10.1023/a:1018860909826.

[17] U. R. Evans, The laws of expanding circles and spheres in relation to the lateral growth of surface films and the grain-size of metals, Transactions of the Faraday Society 41 (1945) pp. 365–374. doi: 10.1039/TF9454100365.

[18] J. W. Christian, *The theory of transformation in metals and alloys*. Pergamon Press (2002).

[19] D. Poquillon and D. Monceau, Application of a simple statistical spalling model for the analysis of high-temperature, cyclic-oxidation kinetics data, Oxidation of Metals 59 (2003) pp. 409–431. doi: 10.1023/A:1023004430423.

[20] Wolfram Research Inc., Mathematica, version 8.0, Champaign, IL, 2010.

[21] M. Halvarsson, J. Tang, H. Asteman, J.-E. Svensson and L.-G. Johansson, Microstructural investigation of the breakdown of the protective oxide scale on a 304 steel in the presence of oxygen and water vapour at 600 °C, Corrosion Science 48 (2006) pp. 2014–2035. doi: 10.1016/j.corsci.2005.08.012.

[22] M. G. C. Cox, B. McEnaney and V. D. Scott, Phase interactions in the growth of thin oxide films on iron-chromium alloys, Philosophical Magazine 29 (1974) pp. 585–600. doi: 10.1080/14786437408213241.

[23] C. Leygraf and G. Hultquist, Initial oxidation stages on Fe–Cr(100) and Fe–Cr(110) surfaces, Surface Science 61 (1976) pp. 69–84. doi: 10.1016/0039-6028(76)90408-8.

[24] G. Hultquist, B. Tveten and E. Hörnlund, Hydrogen in chromium: Influence on the high-temperature oxidation kinetics in H_2O, oxide-growth mechanisms, and scale adherence, Oxidation of Metals 54 (2000) pp. 1–10. doi: 10.1023/A:1004610626903.

[25] S. Henry, J. Mougin, Y. Wouters, J.-P. Petit and A. Galerie, Characterization of chromia scales grown on pure chromium in different oxidizing atmospheres, Materials at High Temperatures 17 (2000) pp. 231–234. doi: 10.1179/mht.2000.17.2.008.

[26] M. Michalik, M. Hänsel, J. Zurek, L. Singheiser and W. Quadakkers, Effect of water vapour on growth and adherence of chromia scales formed on Cr in high and low p_{O_2}-environments at 1000 and 1050 °C, Materials at High Temperatures 22 (2005) pp. 213–221. doi: 10.1179/mht.2005.025.

[27] P. K. Footner, D. R. Holmes and D. Mortimer, Oxidation of iron-chromium binary alloys, Nature 216 (1967) pp. 54–56.

[28] G. C. Wood, I. G. Wright, T. Hodgkiess and D. P. Whittle, A comparison of the oxidation of Fe–Cr, Ni–Cr and Co–Cr alloys in oxygen and water vapour, Materials and Corrosion 21 (1970) pp. 900–910. doi: 10.1002/maco.19700211105.

[29] J. Webber, Oxidation of FeCr alloys in O_2/3% H_2O, Corrosion Science 16 (1976) pp. 499–506. doi: 10.1016/S0010-938X(76)80027-3.

[30] D. J. Young, *High Temperature Oxidation and Corrosion of Metals*. Elsevier Corrosion Series Elsevier (2008).

[31] R. A. Holm and H. E. Evans, The resistance of 20Cr/25Ni steels to carbon deposition. III. Cold work and selective pre-oxidation, Materials and Corrosion 38 (1987) pp. 219–224. doi: 10.1002/maco.19870380502.